

# **Chemically Selective Transport in a Cross-linked $H_{II}$ Phase Lyotropic Liquid Crystal Membrane**

Benjamin J. Coscia and Michael R. Shirts\*

*Department of Chemical and Biological Engineering, University of Colorado Boulder,  
Boulder, CO 80309, USA*

E-mail: michael.shirts@colorado.edu

## Abstract

The uniform size and complex chemical topology of the pores formed by self-assembled amphiphilic molecules such as liquid crystals make them promising candidates for selective separations. In this work, we observe transport of water, sodium ions and 20 small polar solutes within the pores of a lyotropic liquid crystal (LLC) membrane using atomistic molecular simulations. We find that the transport of a species is dependent not only on molecular size, but on chemical functionality as well. The membrane's inhomogeneous composition gives rise to radially dependent transport mechanisms with respect to the pore centers. We observe that all solutes perform intermittent hops between lengthy periods of entrapment. Three different trapping mechanisms are responsible for this behavior. First, solutes that drift out of the pore can become entangled among the dense monomer tails. Second, solutes can donate hydrogen bonds to the monomer head groups. Third, solutes can coordinate with sodium counter ions. The degree to which a solute is affected by each mechanism is dependent on the chemical functionality of the solute. Using the insights developed in this study, we can begin to think about how to redesign existing LLC membranes in order to perform solute-specific separations.

## 1 Introduction

Membranes capable of separating nm-sized solutes with high selectivity and permeability are highly desirable for a number of applications. For example, separation of salt from seawater or other briny sources can yield potable drinking water.<sup>1</sup> Removal of organic micropollutants, such as personal care products, pesticides and pharmaceuticals, from surface and groundwaters, can have large benefits for public health.<sup>2</sup> Finally, one can purify and recover dissolved species present in complex hydraulic fracturing flowback water waste streams which would help mitigate the effects of deep well injection and can be sold for profit.<sup>3</sup>

All of these separations are possible in part with current commercial membrane separa-

tion techniques, but all still suffer from serious drawbacks. Currently, reverse osmosis (RO) and nanofiltration (NF) dominate commercial membrane separations of small molecules.<sup>4</sup> RO membranes are typically dense polymer matrices that separate solutes based on differences in their solubility and permeability in the membrane material.<sup>1</sup> Although they can perform highly selective separations, high feed pressures and thus large amounts of energy are necessary in order to generate a useful permeate flux.<sup>5</sup> NF membranes have well-defined nm-sized pores which can give the same permeate flux as RO with lower applied pressure.<sup>6</sup> However, the pores are not uniform in size, limiting their selectivity.<sup>7</sup>

Under the right conditions, amphiphilic molecules can self-assemble into ordered nanostructures that may be capable of performing highly selective separations with permeabilities comparable to NF.<sup>8</sup> The uniform-sized aqueous pores characteristic of these types of systems enforce a molecular-size cut-off, eliminating issues related to the polydispersity of NF pores.<sup>9</sup> In addition to size-exclusion, it may be possible to control the chemical environment within the nanopores by altering the identities of the hydrophilic moieties that form the pores, affording solute-specific separations.<sup>10</sup>

Amphiphilic lyotropic liquid crystals (LLCs) are known to form the type I bicontinuous ( $Q_I$ ) and inverted hexagonal ( $H_{II}$ ) phases.<sup>3,11–13</sup> When cross-linked, these materials can function as mechanically strong separations membranes.<sup>9</sup> The  $H_{II}$  phase has hexagonally packed, straight pores which is the ideal geometry for high throughput separations. However, the synthesis of  $H_{II}$  membranes with highly aligned hexagonal mesophases has been a challenge that has been met with limited success and has prevented the material's viability as a separations membrane.<sup>?</sup> The  $Q_I$  consists of a three dimensional network of tortuous and interconnected pores. It's more facile synthesis has yielded it more success. The latest  $Q_I$  phase membranes have been shown to exhibit selectivities higher than commercial NF and RO membranes permeabilities higher than commercial RO membranes.<sup>3</sup>

Although  $Q_I$  membranes have shown promising results, it is not clear how to controllably design them for specific separations beyond what has already been achieved. Dischinger

et al. found that they do not separate purely on the basis of size. Empirical modeling revealed correlations between various solute physicochemical properties and observed solute rejection. Although there was some agreement with their empirical model, it does not offer a sufficiently detailed explanation of governing molecular interactions.<sup>10</sup>

Molecular dynamics (MD) simulations can give us mechanistic insights with atomistic resolution so that we can provide detailed descriptions of small solute transport within LLC membrane nanopores and intelligently design new membranes for solute-specific separations. In our previous work, we used MD simulations to determine the most likely structure of the hexagonal phase formed by the monomer Na-GA3C11, expanding upon the most recent experimental characterization.<sup>7,8</sup> We developed techniques to simulate the hexagonal phase formed by neat monomer as well as with varying amounts of water in the pores.

In this work, we present studies of the transport mechanisms exhibited by 20 uncharged polar solutes with varying size, chemical functionality and hydrophilic character within the pores of an H<sub>II</sub> phase LLC. The pores of the H<sub>II</sub> phase have a similar topology to the Q<sub>I</sub> phase but is a simpler geometry to model. In future studies, we will extend our techniques to the Q<sub>I</sub> phase.

Figure 1 shows an atomistic rendering of the membrane in which we placed solutes. We have listed the solutes studied along with the abbreviations that we will use in the charts for the remainder of this paper in Table 1. Note that, in order limit our studies to uncharged species, we have only studied acetic acid in its protonated form. The pKa of gallic acid is 4.40 while the pKa of acetic acid is 4.75.<sup>14,15</sup> Assuming that the pKa of gallic acid is similar to NaGA3C11, it is possible for our sodium salted monomer to exist at the same time as protonated acetic acid. In any case, we are more interested in mechanisms of interaction with specific chemical functionality more than the behavior of specific molecules.

We first address the structure of the membrane nanopores. Previously, we studied dry membrane systems and some systems with low water content. We showed that those systems have rather crowded pores with high concentrations of monomer head groups, sodium ions

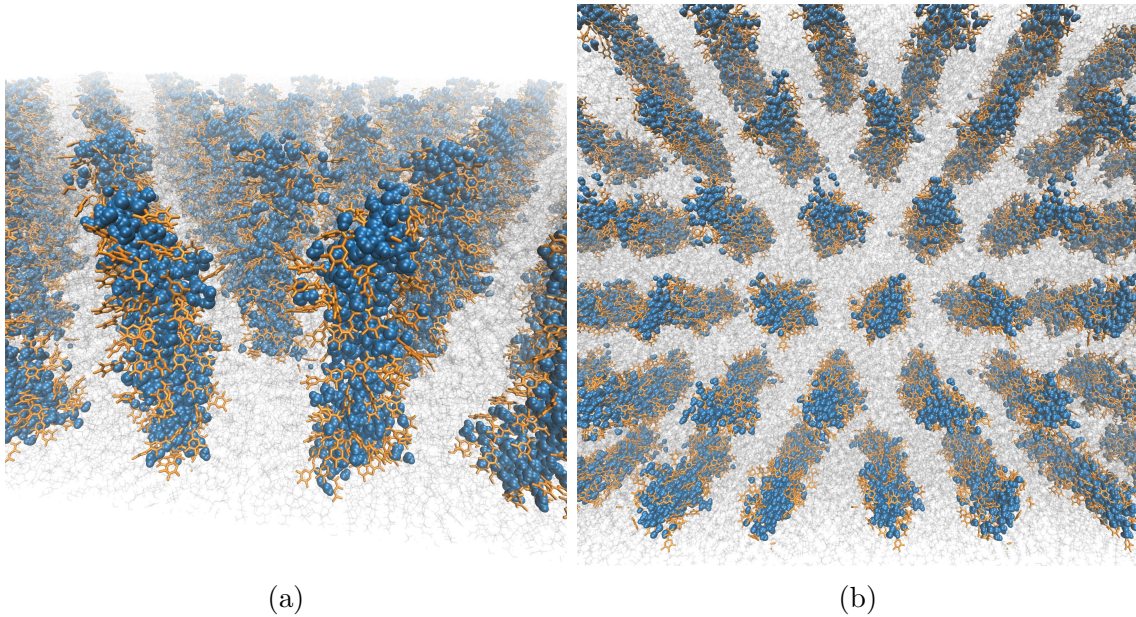


Figure 1: The H<sub>II</sub> phase formed by LLC monomers consists of pores that are approximately straight (a) and packed hexagonally (b). In both figures, water molecules that occupy the pores are colored blue, the hydrophilic head groups of the LLC monomers are colored orange and all else is colored gray. The chemical environment within the nanopores is largely determined by the functionality of the head groups. Additionally, there is not a well-defined transition point from the aqueous pore region to the alkane-dense, hydrophobic tail region, generating further complexity.

**Table 1:** Names of solutes along with their molecular structures and the abbreviations which we use in this paper. Colors correspond to solute groupings and are used in many plots.

Solute Name	Abbreviation	Structure	Solute Name	Abbreviation	Structure
methanol	MeOH		urea	URE	
ethanol	EtOH		acetamide	AcN	
propanol	PrOH		acetone	ACE	
butanol	BtOH		mercaptoethanol	ME	
ethylene glycol	EG		dimethyl sulfoxide	DMSO	
propylene glycol	PG		2,3-dimercapto-1-propanol	DMP	
glycerol	GLY		tetrahydrofuran	THF	
tetrose	TET		dimethylformamide	DMF	
ribose	RIB		propylene carbonate	PC	
acetic acid	AcOH		ethyl acetate	EAC	

and water, where applicable. Here we build systems with appreciable amounts of water, 5 and 10% by weight, and analyze how the radial density of monomer components and water change compared to our previous results.

We then use the transport rates of water in and out of the pores in order to justify our study of solute transport restricted to the pore region. From a macroscopic perspective, it might make sense to hypothesize that water spends its time exclusively in the tube-like

hydrophilic pore region. Our previous work showed that there is a gradual compositional transition from the hydrophilic to the hydrophobic region which means that solutes may not necessarily stay confined to the centers of the pores or even within the pore region. We show that, in our most viable system, water moves fastest within the pores suggesting that the area in and around the central pores should be the focus of our mechanistic studies.

In the remainder of the paper, we describe and quantify three trapping mechanisms which give rise to subdiffusive solute transport behavior. We describe the differences in solute motion, specifically their mean squared displacement (MSD), in conjunction with each solute's size and chemical functionality. We show how distinct interactions with various monomer components as well as membrane water content hinders the motion of solutes. We discuss how the interactions between specific solutes and the membrane depend on the solute's chemical functionality.

There are also several questions beyond the scope of this study. First, we will not study the concentration dependence of the observed transport rates. Although the average MSD might change with concentration, we are focused on the underlying solute-membrane interactions that lead to the observed transport mechanisms which we conjecture will remain roughly the same regardless of concentration. Second, we will not study the chemical potential of solutes in the pores, which could give us a better understanding of equilibrium solute partitioning. However, this information is likely not needed to understand the principal mechanistic details in various membrane regions. This work instead represents a starting point for observing the types of interactions that occur between isolated solutes and the membrane.

## 2 Methods

Python scripts used to set up systems and conduct post-simulation trajectory analysis (as described below and in the supporting information) are available online at <https://github.com/shirtsgroup>

The appropriate scripts to use for the subsequent calculations are summarized in Table S1 of the Supporting Information. We ran all MD simulations and energy minimizations using GROMACS 2018.3.<sup>16–19</sup>

## 2.1 Solute Parameterization

We parameterized the interaction potential for the monomer and solutes using the Generalized AMBER Force Field (GAFF)<sup>20</sup> with the Antechamber package<sup>21</sup> shipped with AmberTools16.<sup>22</sup> We use GAFF as it has been used extensively for use with organic molecules. We assigned atomic charges using the am1bccsym method of `molcharge` included with QUACPAC from OpenEye Scientific Software.

## 2.2 System Setup

Stable H<sub>II</sub> phases, assembled with Na-GA3C11, can be formed using a broad range of water concentrations. In the literature, the system studied in this work is typically synthesized with close to 10 wt% water.<sup>11,23</sup> However, Resel et al. noted that the system is likely fully hydrated with less than 7 wt% water.<sup>24</sup> Excess water fills space between hexagonal mesophases. We decided to test systems with two different water contents: 5 and 10 wt%.

We observed that some water partitions into the distal tail region of our system and therefore built our initial configurations with water in both regions, close to the expected equilibrium partition (see Section S2 of the Supporting Information). We define the distal tail region to be ca. 1.5 nm from the pore center based on the minimum in the radial distribution of water (see Section 2.11). The amount of water present in the distal tail region may or may not be experimentally consistent but it is necessary for our results to be thermodynamically consistent; otherwise, water would slowly leak from the pore into the tail region over several hundred nanoseconds. We iteratively adjusted the pore radius in our systems until the appropriate amount of water fit in the pores after running the GROMACS command `gmx solvate`. We placed water molecules in the distal tail region one at a time in

random locations with a short energy minimization between each insertion. When studying transport of water in the pores, we limited the calculations to water molecules that spent greater than 95% of their time outside of the distal tail region. We justify this decision with better context in Section 3.2.1.

We equilibrated an initial solvated configuration before adding solutes. First, we equilibrated the initial configuration using the ‘wet’ equilibration procedure described in our previous work. Then we cross-linked the equilibrated solvated configuration using the cross-linking procedure also described in our previous work.<sup>25</sup>

To study a given solute, we added 6 solute molecules, equally spaced in  $z$ , to the center of each pore of the equilibrated cross-linked configuration, for a total of 24 solute molecules. We chose 6 solutes per pore to provide a balance of a useful amount of data for generating statistics and a low degree of interaction between solutes (see Section S3 of the Supporting Information). At each insertion point we placed a randomly oriented solute molecule then ran a short energy minimization. We allowed the solutes to equilibrate for 5 ns using Berendsen pressure control then collected transport data over the course of 1  $\mu\text{s}$  MD simulations with pressure controlled by the Parrinello-Rahman barostat.

### 2.3 Mean Squared Displacement

We measured the time-averaged  $z$ -direction (parallel to the pores) mean squared displacement (MSD) of the centers of mass (COM) of each solute over the course of 1  $\mu\text{s}$  MD simulations using Equation 1:

$$\overline{z^2(\tau)} = \frac{1}{T - \tau} \int_0^{T-\tau} (z(t + \tau) - z(t))^2 dt \quad (1)$$

where  $\tau$  is the time lag and  $T$  is the length of the trajectory.<sup>26</sup> The MSD, in standard treatments, grows according to Equation 2:

$$\langle z^2(t) \rangle = K_\alpha t^\alpha \quad (2)$$

where  $\alpha$  is the anomalous exponent and  $K_\alpha$  is the generalized diffusion coefficient. A value of  $\alpha < 1$  indicates a subdiffusive process, while a value of  $\alpha = 1$  and  $\alpha > 1$  is characteristic of Brownian and superdiffusive motion respectively. In practice,  $\alpha$  corresponds to the growth of the *ensemble* MSD given by Equation 3:<sup>26</sup>

$$\langle z^2(t) \rangle = \langle z(t) - z(0) \rangle \quad (3)$$

Since the ensemble MSD is calculated with respect to a reference position, it carries some dependence on its starting point. The time-averaged MSD averages over all possible time lags of a given length, effectively eliminating any initial configuration dependence and generating an increased number of observations. For ergodic systems, both types of MSDs will be equal. Since we have a small number of solutes with which to generate statistics and because we are not calculating values of  $\alpha$  for this particular study, we will only use the time-averaged MSD.

We fixed the length of each simulated trajectory so that we could compare the total MSD between different solutes without the influence of the ageing phenomenon. In systems such as ours where solutes show hopping behavior between long periods of immobility, ageing is defined by the tendency of the average slope of an MSD curve to decrease as the length of trajectories are increased.<sup>27</sup> Since the maximum measured dwell time can be no longer than the total length of a simulated trajectory, longer dwell times are incorporated into the calculation as measurement time or trajectory length is increased, lowering the average MSD. Because the solute MSDs are non-linear and because of the ageing phenomenon, we did not attempt to calculate a diffusion constant as one might for a Brownian particle with a

linear MSD. Instead, the reported MSD values represent the average MSD for a given solute after a 400 ns time lag. Our results are shown to be insensitive to our choice of time lag in Section S4 of the Supporting Information.

The  $z$ -direction MSD of water in the 10 wt% system *is* linear to within statistical precision. Therefore, for the purpose of comparison, we calculated its diffusion constant by fitting a line to the linear region of the MSD curve.<sup>28</sup> The diffusion constant is then equal to  $m/2$  where  $m$  is the slope of the linear fit. The slope is divided by 2 (rather than 6) because we only measured particle displacement in one dimension.

## 2.4 Molecular Size Determination

In order to determine an effective radius for each solute, we divided in half the maximum pairwise distance between atoms of each solute over the course of a 2.5 ns simulation of solutes dissolved in a cubic box of water. Each box consisted of about 2100 water molecules and 6 solutes. Although there exist more involved methods for determining the hydrodynamic radius,<sup>29</sup> we chose to use a simpler and more intuitive metric since we are only interested in observing trends in the solute MSD as a function of solute size.

## 2.5 The Stokes-Einstein Relationship

The Stokes-Einstein relationship expresses the diffusion coefficient of a hard spherical particle as a function that is inversely related to the particle's radius:

$$D = \frac{k_b T}{6\pi\eta f r} \quad (4)$$

where  $k_b$  and  $T$  are the Boltzmann constant and the system temperature respectively and  $\eta$  is the system's viscosity. Here we have also included the microfriction correction factor,  $f$ , introduced by Gierer and Wirtz<sup>30,31</sup> for when solute size becomes on the order of solvent size since the solute can no longer be treated as a non-interacting hard sphere.  $f$  is defined

in terms of the ratio of  $r_1$  and  $r_2$ , the radii of the solute and solvent molecules respectively:

$$f = \left( 1.5 \frac{r_2}{r_1} + \frac{1}{1 + \frac{r_2}{r_1}} \right)^{-1} \quad (5)$$

For consistency with the presentation of our results, rather than calculate trends in  $D$ , we will calculate trends in trends in solute MSDs. For Brownian particles,  $D$  is proportional to the MSD divided by time,  $t$ . Therefore, we analyze qualitative trends in solute MSDs according to:

$$MSD = \frac{k_b T t}{6\pi\eta f r} \quad (6)$$

We hold  $t$  constant in our simulations in order to make side-by-side comparisons.

Since we will be using Equation 6 for primarily qualitative observations, we made a number of simplifying assumptions so that it could easily be used for comparison between systems. First, we assume that all systems' viscosities are equal since we only make minor changes to the membrane's composition and accurately assessing the viscosity in a complex and inhomogeneous system such as ours is a challenge by itself. Second, we assume all particles are approximately spherical, neglecting the effect of solute shape on mobility. Chan et al. showed that the difference in diffusion constants of differently shaped particles, with constant molecular volume, did not differ by more than 25% with most deviating by less than 10%.<sup>32</sup> Third, we assume that the ratio of solute and solvent radii as calculated using the methodology of Section 2.4, is equivalent to the the ratio of hydrodynamic radii. For similarly shaped molecules, it has been shown that one can relate the hydrodynamic radius and radius of gyration ( $R_g$ ) using a constant scaling factor.<sup>33–35</sup> Assuming that our end-to-end distance reasonably approximates  $R_g$  for our small, relatively inflexible molecules, we believe this assumption is justified for qualitative demonstrations relevant to this study.

In order to make qualitative comparisons, we fit Equation 6 so that it passed through the highest solute MSD. We assumed that the solute with the highest MSD exhibited the

closest to Brownian behavior and therefore could set a rough boundary between subdiffusive, Brownian and superdiffusive MSDs. As a lower bound to our appoximation, we also plotted the uncorrected version of Equation 4 ( $f=1$ ), requiring it to converge to the same value as the corrected curve for large radii.

## 2.6 Hop Detection

In order to measure the length of hops, we first needed to detect when they occurred. We used an off-line change point detection algorithm, implemented in the python package `ruptures`,<sup>36</sup> in order to determine at which points hops occurred in the time series of each solutes' COM. We used the 3 dimensional COM positions of each solute, rather than just the  $z$ -direction, in order to detect lateral hops. However, hop lengths are reported as their displacement in the  $z$ -direction. We reported the standard error in the average hop lengths by bootstrapping the empirical distribution of observed hop lengths.<sup>37</sup>

We determined the average frequency of hops by dividing the total number of hops by the total length of the simulation. We used the frequency of hops per 1000 ns as the  $\lambda$  parameter in a Poisson distribution. We calculated the  $1\sigma$  confidence intervals of the probability distribution of hops per 1000 ns based on the corresponding Poisson cumulative distribution function and scaled them to a per-nanosecond basis.

We differentiated between the length of hops inside and outside of the pores. For 10 wt% water systems, we consider a solute to be in the pore if it is within 0.75 nm of a pore center. This radial cut-off maximizes the difference between average hop lengths in and out of the pore. See Section S5 of the Supporting Information for further details on this optimization.

## 2.7 Time Spent in Pore Region

Using the cut-off defined above, we calculated the fraction of time that a solute spends within the pore region. Since this is a process with two possible outcomes, we calculated the

standard error ( $SE$ ) of our calculations based on the binomial theorem:

$$SE = \sqrt{\frac{p(1-p)}{n}} \quad (7)$$

where  $p$  is the probability that a solute is in the pore region and  $n$  is the sample size. Here  $n$  is the total number of transitions between each region.

## 2.8 Identification and Analysis of Hydrogen Bonds

Based on the geometric criteria proposed by Luzar and Chandler,<sup>38</sup> we determined a hydrogen bond to exist if the distance between the donor, D, and acceptor, A, atoms is less than 3.5 Å and the angle formed by D–H $\cdots$ A is less than 30°. Attempts to describe a hydrogen bond in the context of molecular simulations has yielded a number of definitions with no true consensus<sup>39</sup> especially since the geometry of hydrogen bonds has some dependence on the system being studied. The definition of Luzar and Chandler is easily visualized for trajectories using the `hbonds` representation of the Visual Molecular Dynamics (VMD) software package which allows us to directly check the validity of identified hydrogen bonds. In Section S6 of the Supporting Information, we show that our conclusions are insensitive to this definition within a reasonable range of distances and angles.

We determined the average percentage of solutes which actively participated in a hydrogen bond interaction with monomers each frame. Unless noted otherwise, we only counted unique solute–monomer hydrogen bond interactions, meaning solutes that hydrogen bond more than once simultaneously were classified as a single pairing event. We determined the standard error of this calculation by bootstrapping over each solute’s trajectory. For each bootstrap trial, we randomly chose 24 solutes with replacement and calculated the average active solute–monomer hydrogen bonds per frame.

## 2.9 Coordination Number

We quantified the coordination of solute constituent atoms with sodium ions. For each frame, we counted the number of coordinated molecules to a given solute atom based on a distance cut-off. Using four different methods, Rowley and Roux observed peaks in the radial distribution function for sodium coordinated with water at an O–Na distance of between 2.3 and 2.5 Å.<sup>40</sup> We used 2.5 Å as the distance cut-off in our calculations. We found that this approach is more useful than calculating the 3D spherical radial distribution function because it gives detailed frame-by-frame information rather than an average.

Using our procedure, we found that sodium ions in a solution of TIP3P water coordinate with an average of 3.6 water molecules. We created a 4 x 4 x 4 nm cubic box of water with the GROMACS tool, `gmx solvate`. We used `gmx genion` to replace water molecules with sodium and chloride ions in order to create a 0.1 M NaCl solution. We let the system simulate for 5 ns and reported the average number of coordinated water molecules per frame after discarding the first nanosecond of simulation.

We determined the average percentage of solutes actively coordinated to a sodium ion each frame. Our calculation procedure is analogous to that for solute–monomer hydrogen bond interactions outlined in the previous section.

## 2.10 Association Lifetimes

We quantified the length that two species stay associated via hydrogen bonding or coordination. For each unique pair, we measured the number of consecutive frames in which they stayed associated. We considered pairs that disassociated for a single time step and reformed on the next time step as a single continuous association event. We compiled the length of these events into a distribution of association lifetimes.

Hydrogen bond lifetimes appear to be distributed according to a power law or an exponential function (see Figure S9 of the Supporting Information). A number of researchers provide evidence that supports a power law distribution.<sup>41,42</sup> However, these studies were

done on extremely short timescales relative to ours, outputting positions every time step. Voloshin et al. studied hydrogen bonding on multiple timescales and observed exponential behavior on the longest timescales.<sup>43</sup> Due to memory limitations, we could not collect data frequently enough to provide a sufficient answer to this question so when comparing solutes, we use the 95<sup>th</sup> percentile of hydrogen bond dwell times. This places emphasis on solutes with long dwell times. We reported the standard error of this calculation by bootstrapping the distribution of dwell times.

The distribution of sodium association lifetimes appear similar to hydrogen bond life time distributions. Therefore, we reported association lifetimes in the same manner as hydrogen bond lifetimes.

## 2.11 Radial Distribution Functions

We measured the average radial distance of each solute of interest from the pore centers. We binned the radial distances and then normalized by the volume of the annulus defined by the bin edges. We generated  $1\sigma$  confidence intervals by bootstrapping the RDFs of each individual solute 200 times. For each solute, we obtained an RDF averaged over the entire simulation trajectory. We randomly chose individual solute RDFs with replacement from the set of 24 and averaged each set for each bootstrap trial in order to generate a distribution from which to calculate uncertainties. This approach assumes that solute positions are uncorrelated to other solutes which we believe is valid due to the low degree of interaction between solutes described in Section 2.2.

Although the pores are often described as straight, they have a small degree of tortuosity which disrupts the RDF calculation. We tried to mitigate the effects of tortuosity by calculating the RDF with respect to splines that run through the pore centers. See Section S8 of the Supporting Information for a graphical illustration. Each spline consists of 10 points, equally spaced in the  $z$ -direction, whose  $(x, y)$  coordinates are defined based on the COM of all head groups closest, in  $z$ , to the given point. When calculating RDFs, the radial distance

from the pore center is based on the distance between the solute COM and the linearly interpolated ( $x, y$ ) coordinates of the pore center calculated based on the closest two spline points. Using the splines, we calculated the tortuosity of the pores by calculating the ratio  $\frac{L}{Z}$  where  $L$  is the length of the spline and  $Z$  is the length of the unit cell in the  $z$ -direction. The average tortuosity of each pore is  $1.03 \pm 0.01$  and  $1.07 \pm 0.02$  in the 5 and 10 wt% water systems respectively.

In all RDF plots, we include the average RDF of the head groups as a reference. The head group RDF shown is the average of the head group RDFs for each solute system in the plot. We generated  $1\sigma$  confidence intervals by bootstrapping the RDFs in the same way we did the solutes. We scaled the head group RDF so that it would be in frame next to solute RDFs.

## 3 Results and Discussion

### 3.1 Structure of Membrane Constituents

Before beginning our analysis of solute transport behavior, it is important to elucidate the topology of the membrane pores in solvated systems.

In contrast to our previous work with a dry version of this membrane, the region close to the pore center of the 5 and 10 wt% water systems is primarily filled with water and sodium ions. Figure 2 plots the RDF of each membrane constituent in the dry system as well as the 5 and 10 wt% water systems. In dry systems, the pore center is densely filled with sodium ions and head groups. In hydrated systems, water occupies, and is densest, at the center of each pore. The density of sodium ions is somewhat uniform in the pore center of the 5 wt% water system while it shows a maximum closer to the head groups in the 10 wt% water system. The peak density of sodium ions is not at the pore center in the 10 wt% water system likely because they are associated with the monomer's carboxylate head groups.

Pores in the 10 wt% water system are wider and less crowded by monomers than those in

the 5 wt% water system. The peak head group density of 10 wt% water systems is about 0.2 nm further from the pore center than the 5 wt% water system. Based on these observations, we expect solute transport to be fastest in the 10 wt% water system.

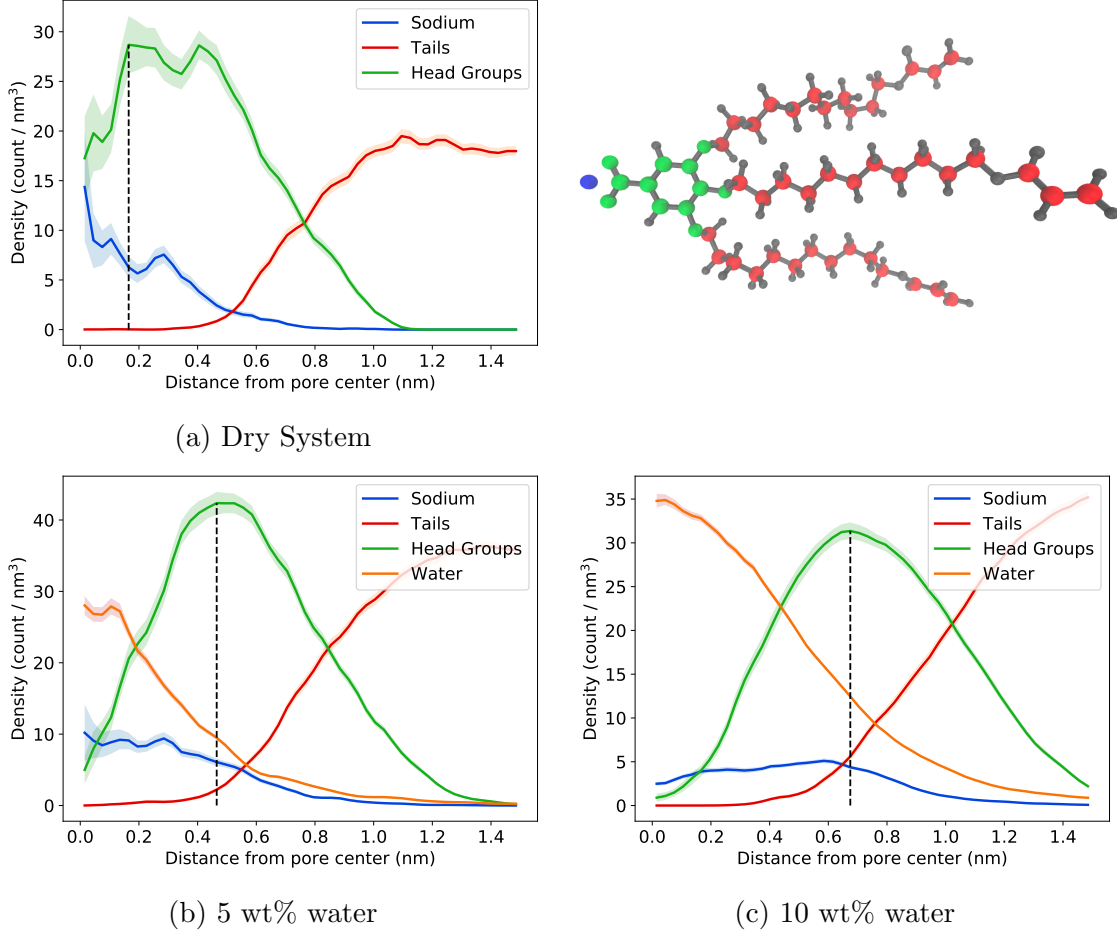


Figure 2: The radial densities of various monomer components paint a picture of the pore topology where the pore centers of hydrated systems are primarily, but not exclusively, composed of water and sodium ions. The monomer groups labeled in each plot correspond to the color-coded monomer pictured in the upper right corner of the figure. RDFs show the average number of atoms located at a given distance from the pore center normalized by the volume of the annular bin to which they belong. The vertical dashed black lines are positioned so that they intersect with the maximum head group density. (a) In the dry system, the density of head groups and sodium ions are highest 0.15 to 0.4 nm from the pore center. There is an appreciable density of head groups crowding the pore center. (b) In the 5 wt% system, monomer head groups retreat radially in order to make room for water molecules at the pore center. (c) Monomers in the 10 wt% system retreat an additional 0.2 nm to make room for more water.

There is an appreciable amount of water that partitions into the distal tail region of

both systems. 28% and 31% of the total water is present in the distal tail regions of the 5 and 10 wt% water systems respectively. See Section S2 of the Supporting Information for more details on the equilibrations that led to this conclusion. The partition is due to a combination of the distal tail region's lower density (see Figure 3) as well as oxygen atoms at the ends of each monomer tail which can further stabilize water molecules.

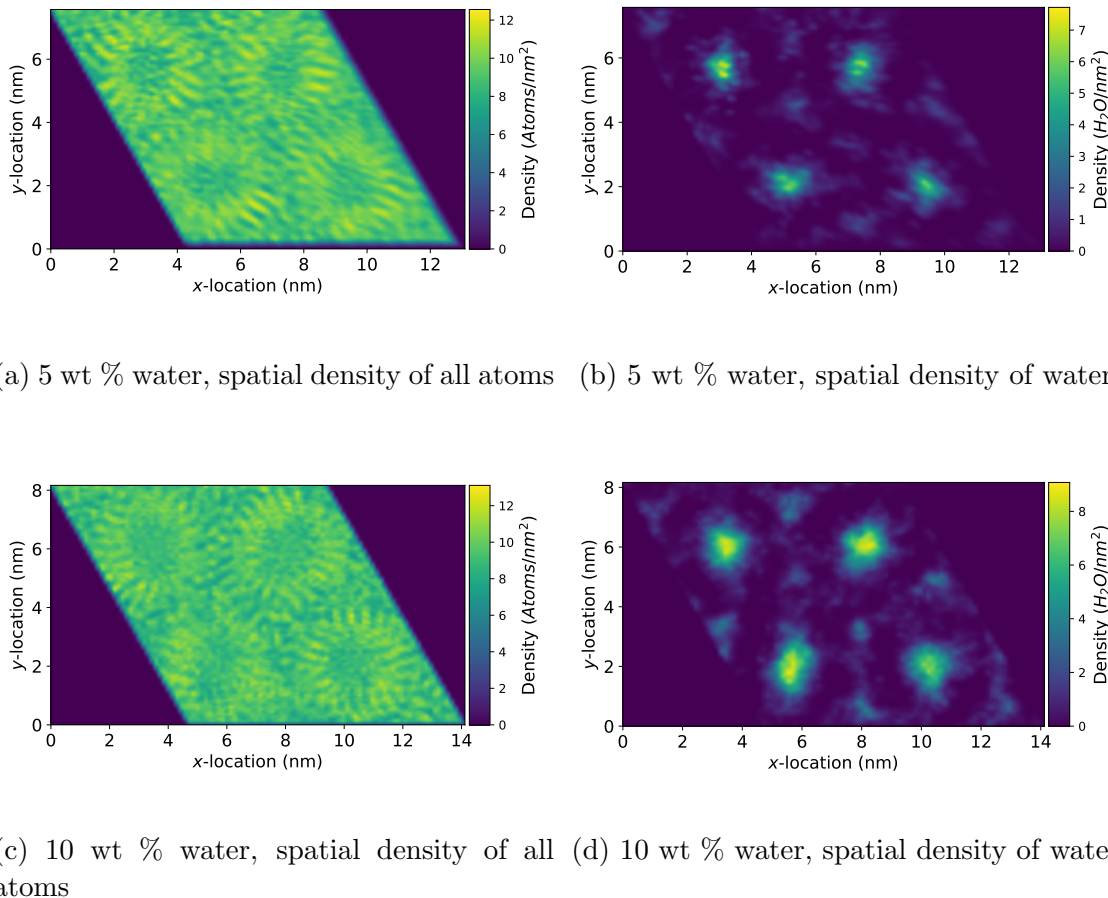


Figure 3: Looking down at the  $xy$  plane of the LLC membranes, the lowest density regions of both membranes are in the pore center and in the tail region, furthest from the pore center (a & c). Water is densest in the low density regions (b & d).

We will restrict our studies of transport to solutes and water outside of the distal tail region because transport is fastest in the pores. We provide more rigorous justification for this restriction at the end of Section 3.2.1.

## 3.2 Mechanisms Governing Small Solute Transport

We observed transport of sodium, water and 20 other small polar solutes inside the membrane nanopores. First, we comment on transport of the membrane constituents, water and sodium, in a system absent of any additional solutes. We then present the general trends that we observe among the all other solutes studied.

### 3.2.1 Water and Sodium Ions

Water and sodium's mobilities increase in larger and less crowded pores. In the 10 wt% water system, the MSD of water is about 51 times higher and the MSD of sodium is about 49 times higher compared to the 5 wt% water system. In the 10 wt% water system, water moves about 51 times faster than sodium and in the 5 wt% system, water moves about 49 times faster than sodium. Due to the linearity of water's MSD in the 10 wt% water system, we assumed long timescale Brownian behavior and measured its diffusivity to be  $7.45 \times 10^{-7} \text{ cm}^2/\text{s}$  which is only 1.4% that of bulk TIP3P water.<sup>44</sup>

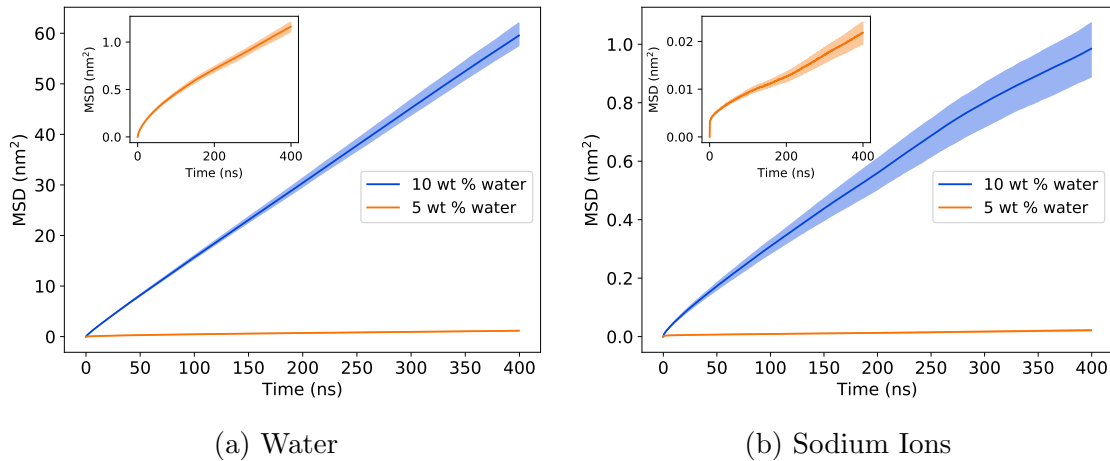


Figure 4: (a) The  $z$ -direction MSD of water in the 10 wt% water system is about 51 times higher than water in the 5 wt% water system. Water appears to exhibit Brownian motion in the 10 wt% system due to its linear MSD. (b) The MSD of sodium in the 10 wt% water system is about 49 times higher than sodium in the 5 wt% water system.

Sodium coordinates with both water and carboxylate moieties from the head groups in the pores. Sodium coordinates with 3.4 water molecules in bulk solution (see Section 2.9),

but on average in the pores, coordinates with 1.7 water molecules in the 10 wt% system and 1.2 water molecules in the 5 wt% system. The sodium ions additionally coordinate with 1 carboxylate group in the 10 wt% water system and 0.8 carboxylate groups in the 5 wt% water system. This behavior likely slows the motion of the sodium ions considerably compared to bulk water.

In the 10 wt% water system, water molecules that spend the majority of their time in the distal tail region move significantly slower than those close to the pore center. In Figure 4a, we constructed the MSD curves based on water molecules that spent > 95% of their time outside the distal tail region. If we instead restrict our calculation to water molecules that spend > 95% of their time *in* the distal tail region, the MSD of water is about 8 times lower, decreasing from 59.6 to 8.2 nm<sup>2</sup>.

In the 5 wt% water system, water molecules that spend the majority of their time in the distal tail region have MSDs slightly higher than those of water molecules close to the pore center. The MSD of distal tail water molecules is 1.7 nm<sup>2</sup> compared to 1.2 nm<sup>2</sup> outside the distal tails. This anomaly is likely a consequence of lower density in the distal tails relative to the pores, leading to faster diffusion in the tails, as well as slowed diffusion of water molecules in the pores via hydrogen bonds with other water molecules and association with sodium ions. Water molecules are less likely to hydrogen bond with each other while in the distal tail region since they are interspersed between chains, while those in the pores stay in close proximity to each other. We observed about 9 times more hydrogen bonding between water molecules near the pore center versus those in the distal tail region. Additionally, an average of 65% of water molecules in the pores of the 5 wt% water system are associated with a sodium ion each frame compared to 44 % in the 10 wt% water system. There is a negligible amount of hydrogen bonds between water molecules and monomer head groups.

Because the MSD of water in the pores of the 10 wt% system is significantly higher than that in the tails, we restrict our studies of transport in this paper to solutes in or near the pore center. Transport of solutes in the pores is likely to be the limiting factor that

determines permeability and rejection. Although tail transport of water in the the 5 wt% water system is faster than pore transport, water transport overall is significantly slower than in the 10 wt% system. For practical applications, a membrane with water transport properties comparable to the 10 wt% system is far more feasible than the 5 wt% system.

### 3.2.2 Transport of Small Polar Solutes

We observe trends in transport properties that are dependent on the chemical environment within the nanopores rather than just solute size. Polar solutes are slowed by interactions between monomer functional groups and ions. A thorough understanding of these interactions will help us to create monomer design principles. We will begin our analysis by considering the collective trends observed across all systems and then focus on subsets of molecules with structural similarities.

As with water and sodium, the MSDs of the solutes studied in this work are significantly larger in the 10 wt% system than those in the 5 wt% water system (see Figures 5a and 5b). The fastest moving solute in both cases, methanol, has an MSD about 175 times larger in the 10 versus the 5 wt% water system. Clearly the equilibrium water content of a given LLC system will determine its viability for real separations.

The MSDs are not solely a function of solute size. We plotted each solute's radius against their MSD in Figures 5c and 5d. Of all the solutes, methanol is likely subject to the least hindrance by the membrane due its small size. Therefore we fit Equation 6 so that it intersects with methanol's average MSD and radius. The uncorrected version of Equation 6 ( $f=1$ ) is plotted and converges to the same value as the corrected form for large radii (see Section 2.5). Although both curves are approximations, they illustrate that the majority of solutes in our study show lower than expected MSDs. In most cases, the predicted MSDs even fall below the conservative uncorrected Stokes-Einstein estimate. It is clear that more complex mechanisms determine the MSDs of these solutes.

On the timescales simulated in our study, solutes exhibit subdiffusive behavior. Figure 6a

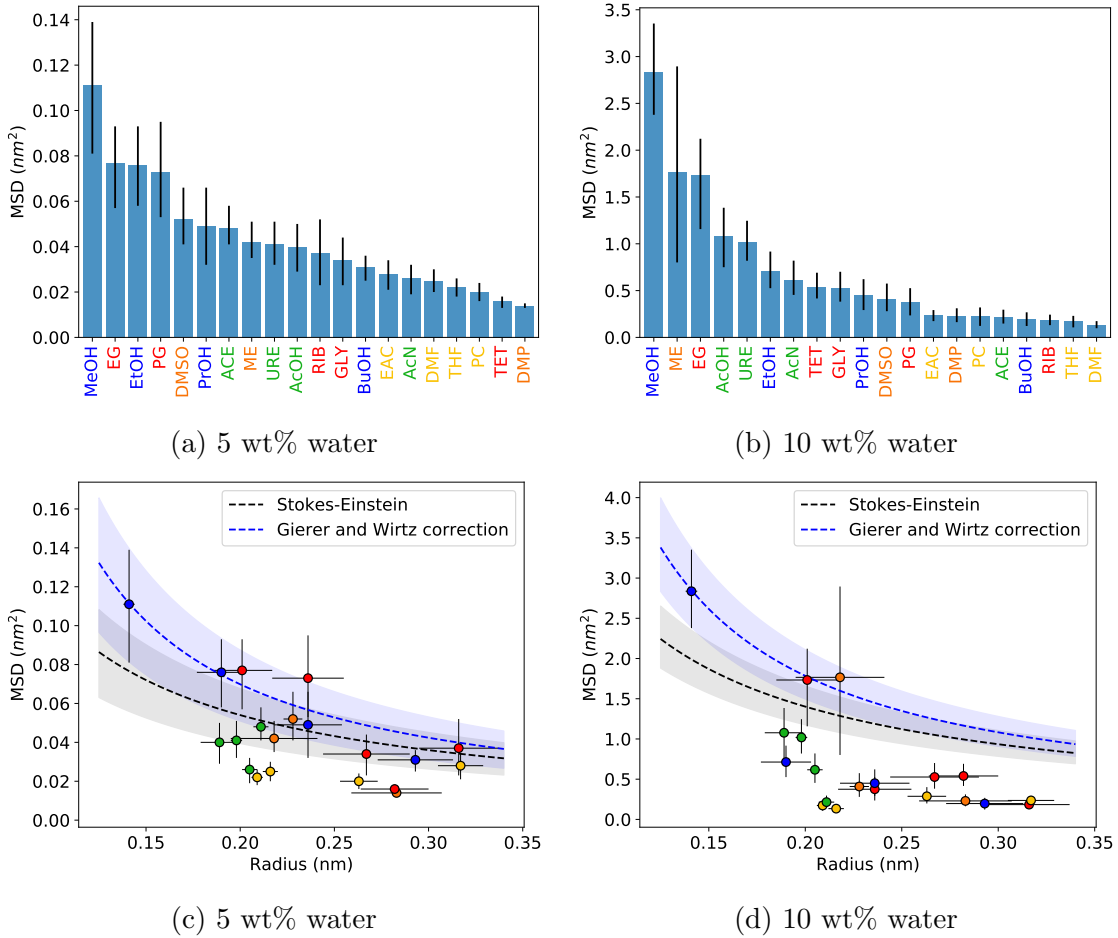


Figure 5: The MSDs of solutes in the 5 wt% water system (a) are significantly smaller than those of the solutes in the 10 wt% water system (b). The MSDs are not a monotonic function of molecular size (c and d). A significant number of solute MSDs fall below the theoretical lines predicted by the Stokes-Einstein equation and Gierer and Wirtz' corrected Stokes-Einstein equation.

plots the  $z$ -coordinate versus time of 3 representative ethanol centers of mass in the 10 wt% water system. There are clear periods of entrapment separated by relatively large hops. The MSD calculated based on all ethanol molecules is plotted in Figure 6b and its shape is sublinear. The long periods of entrapment lead in part to this sublinear, and thus subdiffusive, behavior.

The complex and non-homogeneous structure of the membrane leads to radially dependent transport mechanisms. In general, we observed that hops made in the pore region are about 59% larger than those made outside the pore region (see Figure 7a). There is a high

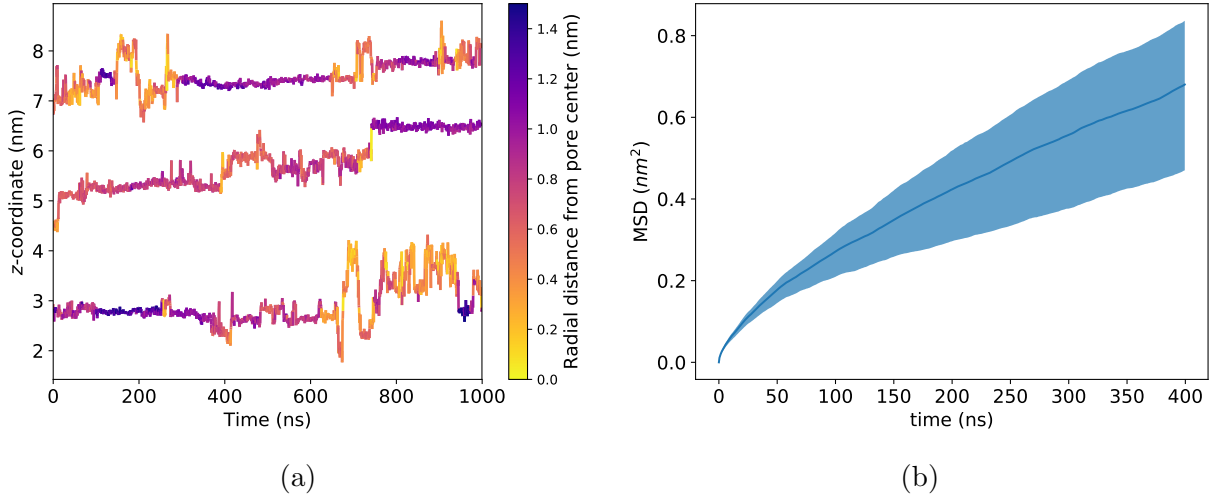


Figure 6: All solutes show subdiffusive transport behavior inside the membrane’s nanopores, similar to that exhibited by ethanol. (a) The  $z$ -coordinate trace of 3 representative ethanol COMs shows clear periods of entrapment separated by hops. In general, the longest dwell times occur when solutes are situated far from the pore center and more frequent hops occur when solutes are close to the pore center. (b) The time-averaged MSD of ethanol is sublinear which suggests transport is governed by an anomalous subdiffusion process.

resistance to movement in the alkane-dense head group and tail regions while, in the pore region, solutes can move relatively freely since it is primarily composed of water molecules. However, time spent in the pore region does not necessarily lead to more frequent hopping. The largest solutes in this study spend the most time in the pore region (see Figure 7b), but many hop with a below-average frequency (see Figure 7c). Therefore, trapping mechanisms controlled by membrane properties other than alkane density must be prevalent.

We observe a second trapping mechanism caused by preferential hydrogen bonding between hydrogen bond donor solutes and monomer head groups. To continue with our ethanol example, we observe that 64% of ethanol molecules donate hydrogen bonds and 3% of ethanol molecules accept hydrogen bonds each frame. On average, 40% of hydrogen bonds donated by ethanol go to carboxylate head groups, 25% go to the ether linkages connecting the monomers tails to the head groups and the remaining 35% to water. There are about 46% less carboxylate oxygen atoms in the pore than there are water molecules yet more hydrogen bonds are donated to them. The stability of hydrogen bonds with carboxylate oxygen atoms

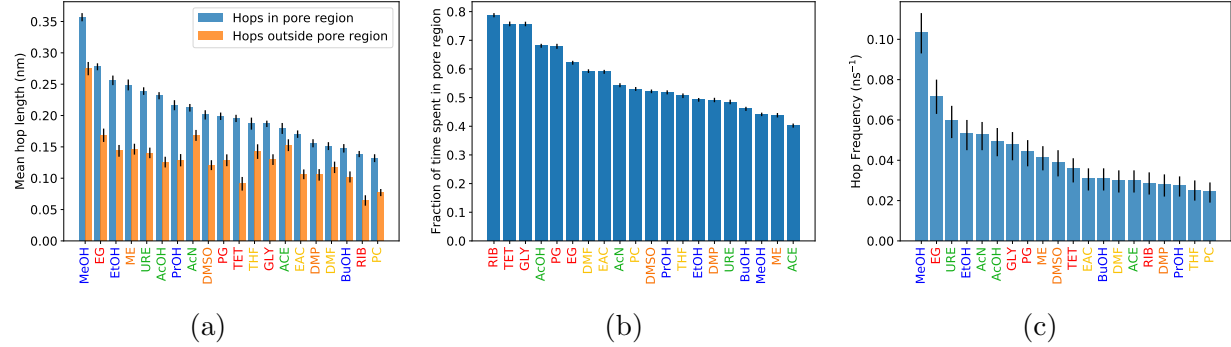


Figure 7: (a) Hops made in the pore region of the 10 wt% water system are, on average, 59% larger than those made outside the pore region. The trend in hop lengths is similar to the trend in MSDs shown in Figure 5b implying that solutes which make consistently larger hops have higher MSDs. The fraction of time spent by a solute in the pore region (b) does not necessarily lead to more frequent hopping (c). For example, ribose spends the largest fraction of time in the pore region, yet hops the fifth least frequently.

is high because they have a negative charge with no neutralizing positive charges nearby. Additionally, on average, each sodium ion is coordinated to 1.7 water molecules meaning an appreciable fraction of the water molecules occupying the pore region are usually coordinated to a sodium ion which decreases their availability to accept hydrogen bonds from solutes.

The lifetime of hydrogen bonds between solutes and monomer head groups tends to be longer for solutes that hydrogen bond more frequently. In Figure 8 we see nearly the same ordering of the percentage of solutes hydrogen bonded to monomer head groups and the 95<sup>th</sup> percentile of hydrogen bond lifetimes. Solutes with multiple hydroxyl groups donate hydrogen bonds most frequently and tend to stay hydrogen bonded longer. Hydrogen bonds donated by nitrogen are far less common and tend to be short-lived as shown by acetamide and urea.

Finally, we observe slowing or immobilization of solutes that associate with sodium counterions. Much like water, the polarity of the solutes creates regions of high electron density, modeled using partial negative charges, which are stabilized through electrostatic interactions with sodium ions. In Figure 9, we've plotted the average percentage of solutes coordinated to a sodium ion each frame as well as the 95<sup>th</sup> percentile of sodium association lifetimes. The degree and length of coordination between solutes and sodium in the 5 wt% water system is

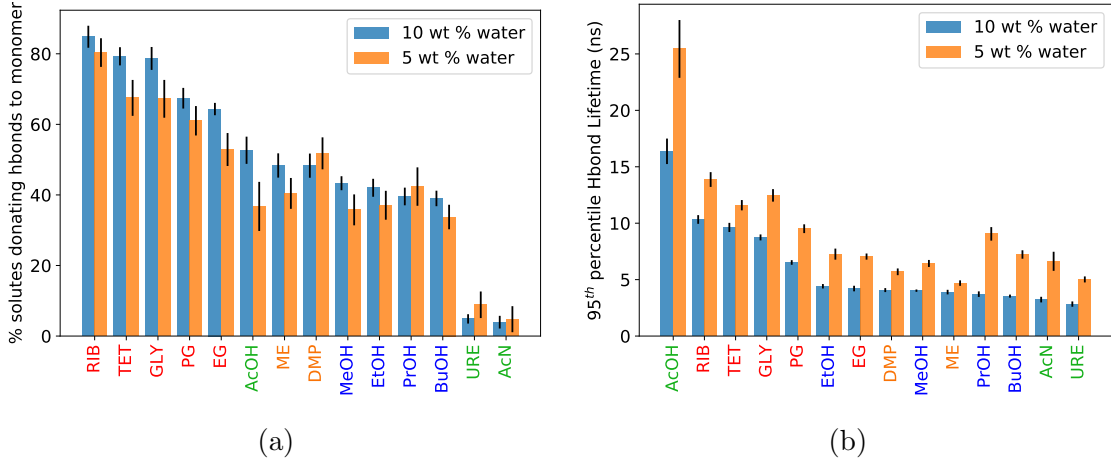


Figure 8: (a) Solutes capable of donating hydrogen bonds to monomer head groups do so to varying degrees. The reported percentages represent unique solute-monomer hydrogen bonds. Individual solutes that hydrogen bond with multiple head groups simultaneously are only counted once. (b) The lifetime of individual hydrogen bonds appears correlated to the percentage of solutes involved in hydrogen bond interactions. Hydrogen bond lifetimes tend to be longer for solutes that hydrogen bond frequently. Note that solutes incapable of donating hydrogen bonds are omitted from this figure.

higher in all cases than that in the 10 wt% water systems. The crowded pores of the 5 wt% water system forces sodium ions in close proximity to solutes.

Carbonyl functional groups tend to associate with sodium the most. Nearly all of the most coordinated solutes contain a carbonyl group (except for DMSO which has an analogous sulfinyl group). There is a significant drop in sodium ion association for solutes that do not contain carbonyl groups or multiple hydroxyl groups to compensate. The corresponding association lifetimes follow a similar trend, however the association lifetimes of highly coordinated solutes with multiple hydroxyl groups are generally lower since association between hydroxyl groups and sodium is apparently a weaker interaction. Carbonyl groups contain an exposed and highly electron-dense oxygen atom which interacts readily with sodium ions. Carbonyl groups with nitrogen substituents appear to interact with sodium more frequently than those with carbon substituents. Acetone associates with sodium significantly less than urea and acetamide.

Coordination of ions with oxygen has been observed in a variety of systems. Carvajal

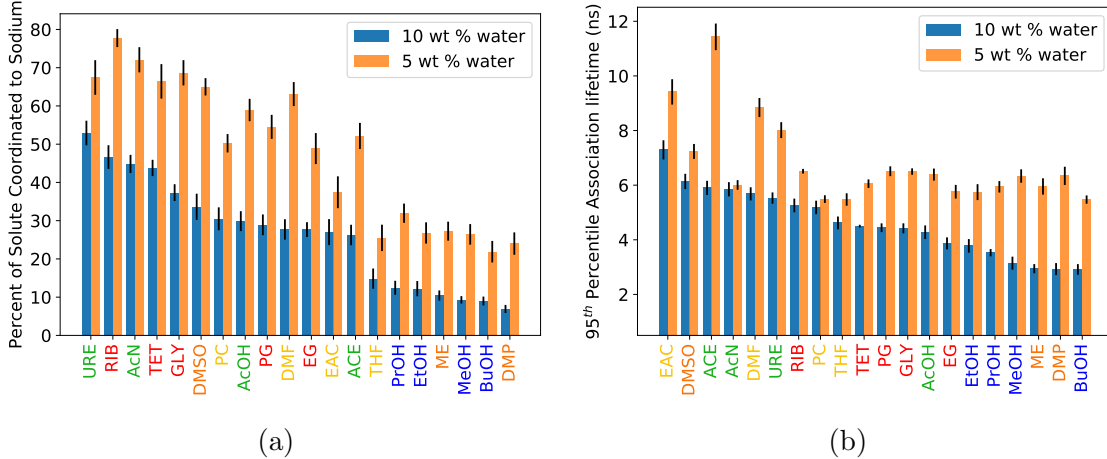


Figure 9: (a) Solutes, especially those with carbonyl groups, spend a significant fraction of time coordinated to sodium ions. (b) The length of time a solute-sodium pairs spends associated tends to be higher for pairs that associate more frequently.

et al. noted that  $\text{Na}^+$  coordinated with four THF molecules when they dissolved a sodium salt in the solvent.<sup>45</sup> Wu et al. observed coordination of  $\text{Na}^+$  with the carbonyl group of a molecule used to design an organic electrode.<sup>46</sup> Finally, Shinoda et al. observed  $\text{K}^+$  ions coordinated with the carbonyl and hydroxyl groups of carboxy-terminal groups in crystallized ATPase.<sup>47</sup>

Overall, the transport behavior exhibited by solutes in the 5 wt% water systems is similar to that shown by those in the 10 wt% system; however the timescales are much longer. We observe subdiffusive behavior with intermittent hopping between periods of entrapment and evidence of the same three trapping mechanisms. The frequency and length of hops are both diminished in the 5 wt% system. Since there are only 24 solute molecules in each system, in order to obtain better time-averaged descriptions of solute transport mechanisms, we will focus the remainder of our analysis on transport in the 10 wt% water systems.

We will revisit our observations in the context of specific groups of molecules in the discussion that follows.

### 3.3 Transport of Simple Alcohols

The MSDs of methanol, ethanol, propanol and butanol descend in order of their size. Using methanol as a reference, the larger alcohols move slower than expected according to both the pure Stokes-Einstein relationship and the corrected relationship (See Figure 10a).

Methanol has the highest MSD of all solutes because it makes the most frequent and longest hops (see Figure 7). Somewhat counterintuitively, methanol, along with the other simple alcohols, spends a smaller fraction of its time in the pore region than most other solutes. However, even outside the pore region, hops made by methanol are larger than those made by almost any other solute in the pore region. The small size of methanol allows it to move relatively unhindered.

The RDFs of longer chain alcohols show a sharp peak near the head groups (see Figure 10b). On average, the density of methanol in the pore center is only slightly less than its density near the head groups while all other alcohol molecules are most concentrated near the head groups.

All simple alcohols participate in a similar number of hydrogen bonding interactions with the monomer head groups, but with varying preference towards hydrogen bonds with the monomer carboxylate oxygen atoms over the ether oxygen atoms that connect the tails to the head groups (see Figure 10c). If all 5 hydrogen bonding acceptor sites on the monomer head groups were equal, we would expect the ratio of the number of hydrogen bonds between solutes and the two carboxylate oxygen atoms to the number of hydrogen bonds between solutes and the three ether groups to be 2/3. There is a clear preference towards hydrogen bonding with the carboxylate oxygen atoms for all simple alcohols. This is largely due to the high net charge of the carboxylate groups as well as the more highly crowded environment surrounding the ether oxygen atoms. Butanol shows the largest preference towards hydrogen bonds with carboxylate head groups. The radial distribution function of atoms located at opposite ends of butanol (Figure 10d) shows that, on average, oxygen atoms are situated closer to the pore centers than the most distal carbon atoms. This suggests that long chain

alcohols will tend to orient themselves like the liquid crystal monomers, with hydrophilic components directed towards the pore centers.

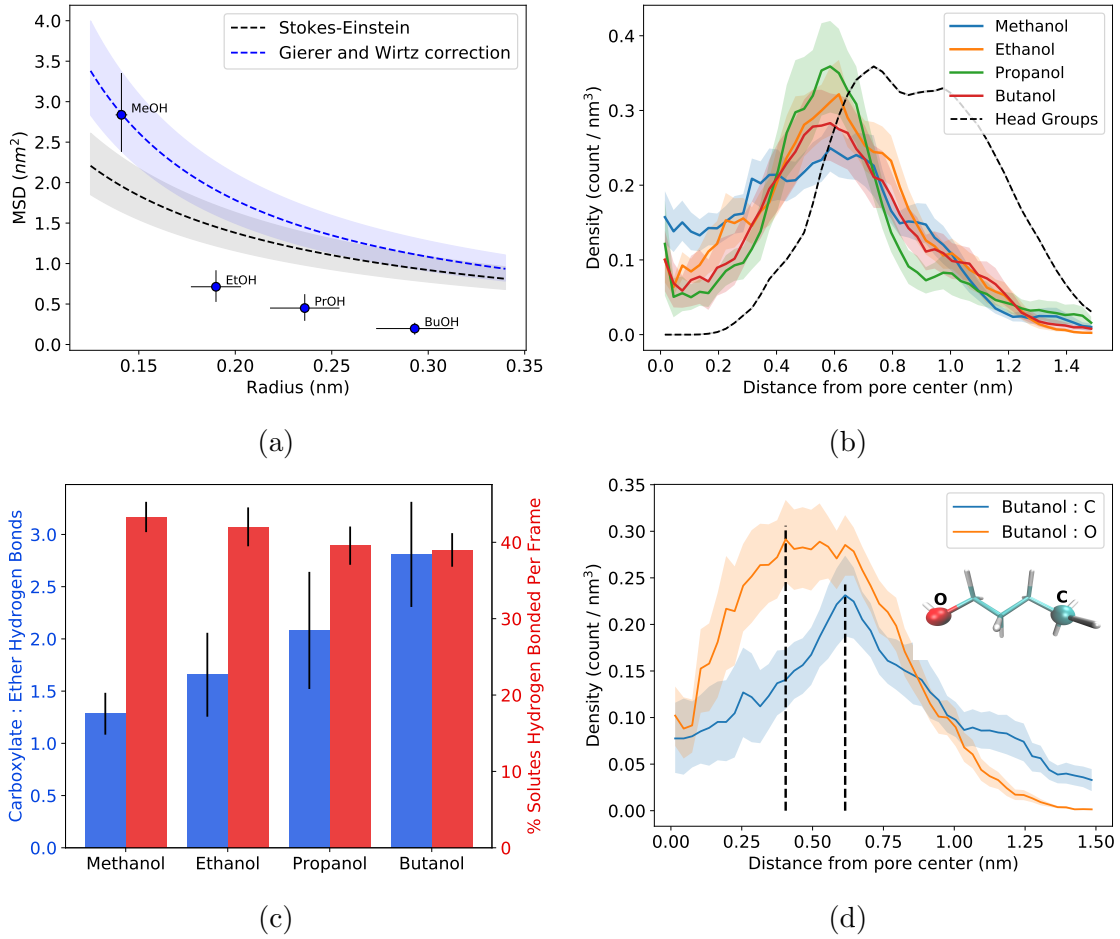


Figure 10: (a) The MSD of the simple alcohols decrease as a function of the solute size, however the MSDs of ethanol, propanol and butanol are considerably lower than expected based on the Stokes-Einstein equation. (b) The radial distribution functions of each simple alcohol shows a maximum close to the highest density of monomer head groups (normalized based on propanol's maximum density for easier visual comparison). Methanol spends the largest proportion of time, relative to the other alcohols, near the pore center, which may help explain its fast dynamics. (c) Despite relatively little difference in the total number of solutes actively participating in a hydrogen bond each frame, a given alcohol's preference towards hydrogen bonds with the carboxylate groups over ether linkages increases with increasing hydrophobic character. (d) The average location of butanol's oxygen atom is closer to the pore center than its most distal carbon atom, suggesting that the molecule is oriented with hydrophobic tails pointing away from the pore center.

### 3.4 Transport of Diols, Triols and Sugars

The order of the MSDs of the diols, triols and sugars are roughly consistent with their size; however, propylene glycol moves exceptionally slowly (see Figure 11a). Ethylene glycol has the highest MSD followed by tetrose and glycerol, whose MSDs are similar, propylene glycol, the second smallest solute of this set, and finally ribose.

Transport is both facilitated and hindered by additional solute hydroxyl groups due to their influence on radial density and hydrogen bond frequency. Extra hydroxyl groups cause solutes to favor the water-rich pore region where there is the least hindrance to movement (see Figure 11b). Tetrose, ribose and glycerol are densest close to the pore center. They spend a greater fraction of their time in the pore region than any other solute (see Figure 7b). This is likely a consequence of both their hydrophilicity and large size which prevents them from partitioning into the head group region. However, these extra hydroxyl groups facilitate a larger number of hydrogen bond interactions that work to hold solutes in place (see Figure 11c). It has been observed that hydrogen bonding in a system will generally reduce diffusivity.<sup>48</sup>

The number of hydrogen bonding interactions between solutes and head groups increases with the number of solute hydroxyl groups. These solutes frequently undergo simultaneous hydrogen bond interactions as shown in Figure 11c. For example, both hydroxyl groups of ethylene glycol can undergo hydrogen bonds with different hydrogen bond acceptors at the same time. In some cases, all 4 hydroxyl groups of ribose hydrogen bond to monomer head groups simultaneously. As a consequence, hydrogen bond lifetimes in these cases tend to be longer (see Figure 8b) since the solute positions are stabilized by multiple interactions. When one hydrogen bond is broken, the remaining unbroken hydrogen bonds keep the molecule in place and allow the previously broken bond to reform. Proximity to the pore center partially compensates for this effect in the cases of glycerol and tetrose, causing them to have relatively high MSDs for their size.

Of the two diols, ethylene glycol moves significantly faster than propylene glycol due

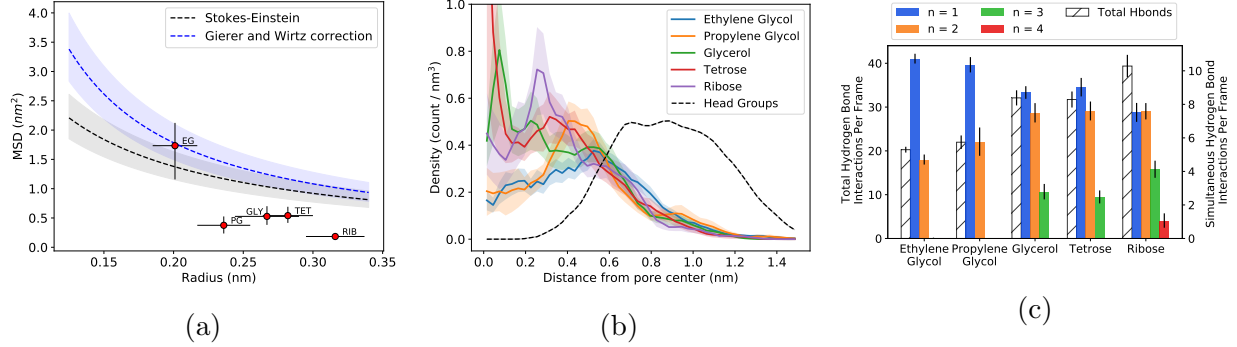


Figure 11: (a) The MSDs of diols, triols and sugars descend in order of their size, except for propylene glycol which moves exceptionally slow. The MSD of ethylene glycol is in close agreement with the theoretical lines, implying that the solute is subject to a similar amount of hindrance as methanol, the solute to which the theoretical lines were fit. (b) Glycerol, tetrose and ribose have high densities close to the pore center because they have a high number of hydrophilic groups and are relatively large. Ethylene glycol and propylene glycol are densest close to the head group region. (c) The number of hydrogen bond interactions between solutes and monomers increases as solutes gain additional hydroxyl groups. The number of hydrogen bonds made by a single solute in different locations simultaneously, n, also increases with the number of hydroxyl groups. In the most extreme case, all four hydroxyl groups of Ribose (n = 4) are involved in a hydrogen bond interaction at the same time.

to propylene glycol's affinity for the monomer head groups. Combined with an increase in size, the addition of a single methyl group to ethylene glycol increases propylene glycol's hydrophobic character and causes it to favor positions near monomer head groups (see Figure 11b). Both diols have comparable densities close to the pore center, however propylene glycol's density has a large peak near the monomer head groups relative to ethylene glycol. Propylene glycol can form more highly stabilized hydrogen bonds with carboxylate groups, explaining the slightly higher incidence of hydrogen bonds shown in Figure 11c. The 95<sup>th</sup> percentile of hydrogen bond lifetimes for propylene glycol with monomers is 9.5 ns compared to 7 ns for ethylene glycol. Somewhat counterintuitively, there is a relatively high density of ethylene glycol molecules beyond the head group region probably due to its relatively small size. This likely contributes to the somewhat large error bars on its MSD in Figure 5.

### 3.5 Transport of Ketones and Amides

The 4 ketone-like molecules tested show a range of transport behaviors. Urea, acetic acid, acetamide and acetone are all characterized by a carbonyl group with two attached heavy atoms. All are similar in size and are planar molecules due to the  $sp^2$  hybridization of their carbonyl group. The fastest solutes of this grouping, acetic acid and urea, move about 3 times faster than the slowest, acetone.

The amides, urea and acetamide, hydrogen bond with head groups relatively infrequently, but regularly coordinate with sodium ions (see Figure 12). In an average frame, over 50% of acetic acid molecules participate in hydrogen bonds with monomer head groups while less than 10% of urea and acetamide molecules hydrogen bond with head groups. Urea and acetamide both have hydrogen bond donating nitrogen atoms, however nitrogen is a weaker hydrogen bond donor than oxygen due to its lower electronegativity.<sup>49</sup> Given their lower propensity to hydrogen bond, one might expect amides to partition out of the pore and/or to move through the pore quickly, perhaps faster than methanol. However, both RDFs contain sharp peaks situated between the pore center and the head groups, but closer to the pore center than other solutes that hydrogen bond with carboxylate groups. Solutes that hydrogen bond frequently tend to show peaks in their RDFs near 0.5-0.6 nm from the pore center (see Figure 10b, for example) and those that coordinate with sodium ions more frequently tend to show peaks in their RDFs near 0.2-0.4 nm from the pore center. Both solutes spend about half of their time with their carbonyl oxygen atom coordinated to a sodium ion which restrains the solutes to within the pore region

Among the solutes in this set, only the carbonyl oxygen atoms coordinate with sodium ions. The nitrogen atoms do not coordinate at all despite a similar negative partial charge because the attached hydrogen atoms shield this interaction by making the NH<sub>2</sub> group approximately neutral.

Acetone has the lowest MSD of this set because it either coordinates with sodium or stays trapped near and behind the head groups. Acetone spends the smallest fraction of

time in the pore region out of all solutes in this study (see Figure 7b). On average, acetone coordinates with sodium with the same frequency as acetic acid which is manifested as a peak in its RDF about 0.2 nm from the pore center. Acetic acid and the amides have other, unoccupied, hydrophilic groups while bound to sodium ions which increases their stability in the pore.

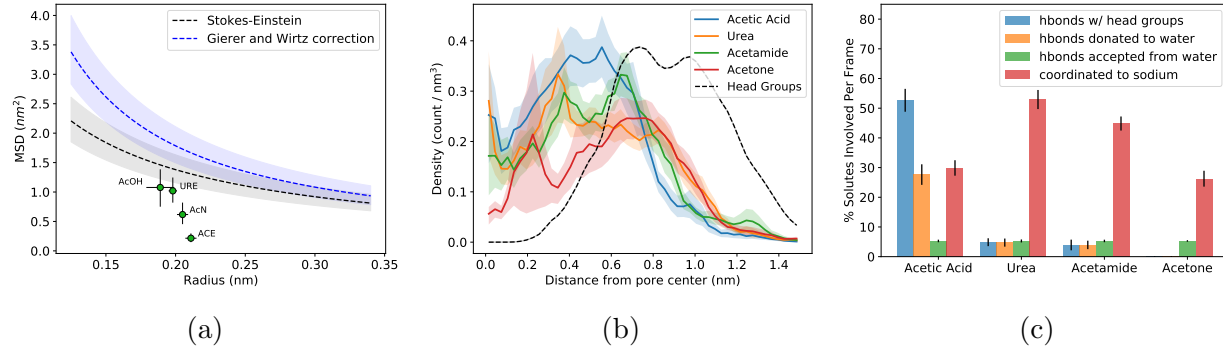


Figure 12: (a) The MSD of ketones and amides decreases and the deviation from Stokes-Einstein predicted behavior increases with molecular size. (b) The radial density near the pore center ( $r = 0$ ) decreases with decreasing solute MSD. Peaks in the RDFs of urea, acetamide and acetone that appear 0.2 - 0.4 nm from the pore center are likely due to coordination with sodium ions. (c) The amides hydrogen bond with water far less than acetic acid, however they tend to coordinate with sodium ions more frequently. Acetone coordinates with sodium with same frequency as acetic acid.

### 3.6 Transport of Thiols

We also studied the transport properties of sulfur analogs of glycerol, ethylene glycol and acetone. We replaced all but one oxygen atom of ethylene glycol and glycerol with sulfur atoms to create dimercaptoethanol and 2,3-dimercapto-1-propanol. We replaced the carbonyl carbon of acetone with sulfur in order to create DMSO. Sulfur-containing compounds form weaker hydrogen bonds than nitrogen and oxygen-containing compounds due to their low electronegativity.<sup>49</sup> For this reason, thiols are less soluble in water than their hydroxyl group analogs.

Mercaptoethanol has a similar average MSD and RDF to ethylene glycol (see Figures 5b and 13b). There is a much larger uncertainty associated with mercaptoethanol's MSD. The

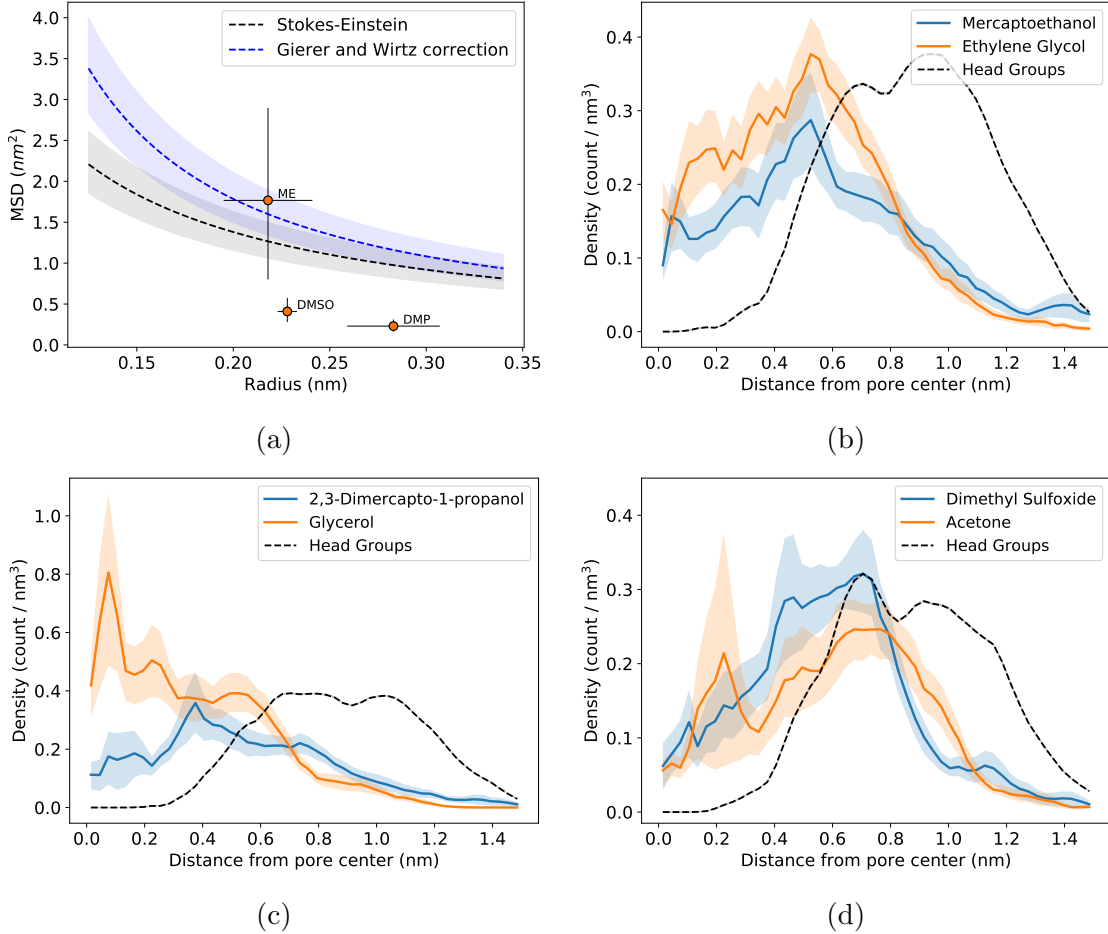


Figure 13: (a) The RDF of mercaptoethanol is similar to ethylene glycol except for its higher density in the tail region and consequently lower density in the pore region. (b) 2,3-dimercapto-1-propanol is densest near the head groups, unlike glycerol whose density is very high close to the pore center. (c) Overall, dimethylsulfoxide has a higher density than acetone within the pore region which may in part explain its marginally larger MSD.

range of behaviors shown by mercaptoethanol help explain the large variance of its MSD. Much can be accounted for by the higher density of mercaptoethanol molecules outside the pore region, where transport is inherently slower. Although both solutes hop with a similar magnitude inside and outside of the pore region, mercaptoethanol spends about 18% less time in the pore region (see Figure 7). This has a large impact on its hop frequency which is 42% lower than that of ethylene glycol. This implies that mercaptoethanol is relatively immobile outside of the pore, but moves quickly inside.

2,3-dimercapto-1-propanol exhibits slower transport than glycerol because more of it par-

titions into the tail region (see Figure 13c). 2,3-dimercapto-1-propanol spends 27% less time in the pore region than glycerol. Glycerol participates in about 2.5 times as many hydrogen bonds as 2,3-dimercapto-1-propanol (including all possible hydrogen bonding groups). Only 22% of the hydrogen bond interactions of 2,3-dimercapto-1-propanol involve sulfur. Because sulfur can only weakly hydrogen bond, 2,3-dimercapto-1-propanol is less soluble than glycerol in the water-filled pores and more readily partitions into the tail region.

DMSO has a comparable MSD to acetone even though it is a larger molecule (see Figure 5). DMSO spends 17% more time in the pore than acetone. On average, 35% of DMSO molecules are coordinated to a sodium ion each frame compared with 26% of acetone molecules. The pyramidal structure of DMSO may force it to spend more time closer to the pore center which increases its interaction with sodium ions. The tendency of DMSO to stay in the pore region counterbalances the sodium ion interactions to give it a higher MSD than acetone.

### 3.7 Solutes Unable to Donate Hydrogen Bonds

The slowest set of molecules we studied can accept hydrogen bonds, but cannot donate them. Among this set are the two slowest solutes in our study: THF and DMF. The MSDs of ethyl acetate, propylene carbonate and acetone are only marginally larger.

The solutes in this set have small hop lengths. 3 of the bottom 6 mean hop lengths are associated with ethyl acetate, propylene carbonate and dimethyl formamide (Figure 7a). Acetone and tetrahydrofuran perform slightly larger hops but with low hop frequencies (see Figure 7c).

The radial density of solutes near the pore center in this set is surprisingly high as shown in Figure 14b. Propylene carbonate and ethyl acetate are among the largest solutes in this study. Their size prevents them from easily entering the tail region and consequently leads to faster transport properties. However, this is not a hard rule. When a solute does overcome the barrier of entry beyond the pore region, it can become trapped. All solutes in this set

show at least a small peak in the pore region which is caused by solutes that get trapped in the tail region for significant periods of time.

Carbonyl groups continue to show high degrees of association with sodium ions. Between 25 and 30% of propylene carbonate, dimethyl formamide and ethyl acetate molecules are coordinated with sodium ions for a given frame which is consistent with the coordination exhibited by acetone (see Figure 14c). The carbonyl group of the amides studied in the previous section associate with sodium nearly twice as frequently as compounds that don't contain nitrogen (see Figure 12c). Association between sodium and solutes in this set are also among the longest, only beaten by other solutes with carbonyl groups and ribose.

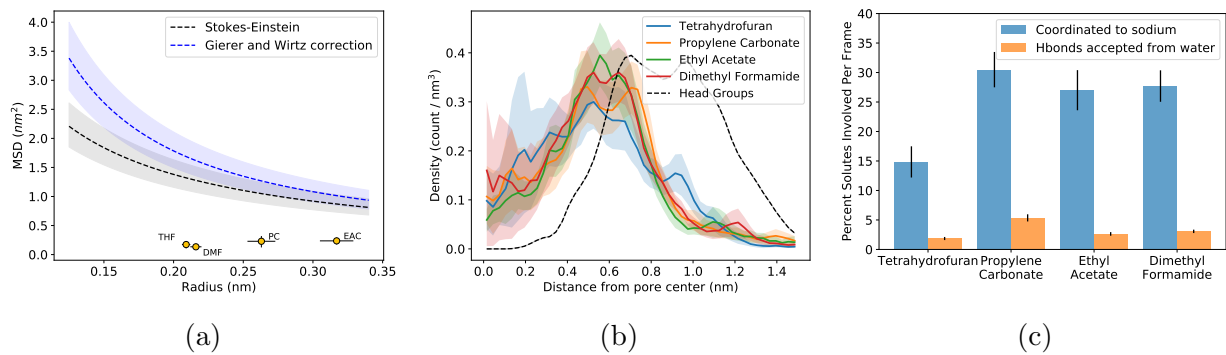


Figure 14: (a) The MSDs of solutes that can only receive hydrogen bonds are significantly lower than expected. (b) The solutes' radial density is surprisingly high in the pore region, but is balanced by an appreciable amount of solute trapped in the tails. (c) The low MSDs exhibited by each of these solutes is due to a combination of entrapment within the tail region and a high degree of coordination with sodium ions.

## 4 Conclusion

We have examined the transport characteristics of a series of small polar molecules in our model of the H<sub>II</sub> phase formed by the liquid crystal monomer Na-GA3C11. We found that transport of solutes is governed by both water content as well as the interplay between the chemical functionality of the solute and the chemical functionality of the LLC monomer and ion making up the pore. We have shown that the MSD of solutes, water and counter ions are highly dependent on LLC membrane water content. As more water is added to the

system, the pores become more dilute in the monomer components. The MSDs of water and sodium ions are nearly 2 orders of magnitude larger in the 10 wt% system than in the 5 wt% system. The amount of water in the pores thus deserves special attention when screening new monomers.

The transport of polar solutes in this system is significantly slower than that of water due to their interaction with the LLC monomers. We observed three primary mechanisms of solute entrapment within the pores.

1. Solutes can become entangled among monomer tails.
2. Solutes can donate hydrogen bonds to immobile monomers.
3. Solutes can associate with counterions.

The chemical functionality of solutes influences the degree to which they are affected by each trapping mechanism. Simple alcohols tend to partition into the tail region as their hydrophobic tail increases in length. Alcohols and sugars with multiple hydroxyl groups are very stable in the pore region, but multiple hydrogen bonds with monomer head groups prevent them from diffusing quickly. This effect is reduced when hydroxyl groups are replaced with thiol groups, but the solutes become less stable in the pore. Finally, solutes with carbonyl groups, which includes the ketones, amides and solutes that can only accept hydrogen bonds, associate with sodium ions, temporarily slowing or immobilizing them.

Based on these trapping mechanisms, we may be able to suggest modifications that can be made to monomers that will modulate their effect on specific solute MSDs in order to make transport even more selective for particular solutes. Since solutes move slowly while entangled among the monomer tails, and since more than half of the solutes studied spend at least 40% of their time in the tails, one can try to design monomers that better control the partition of solutes between the pore and tail region. Solutes move into the tails due both to their size and hydrophilic character. One may be able to contain solutes, even small ones like methanol, by increasing the density of monomers close to the head groups through

incorporation of cross-linkable groups in the vicinity. Alternatively, removal of the ether linkages between the head groups and the monomer tails may decrease the stability of any of the molecules we studied near the head groups and force them to spend more time within the pore.

One could instead focus on designing head groups with varying hydrogen bonding capabilities. Increasing the number of hydrogen bonding sites on the head groups may enhance the membrane's ability to trap solutes like sugars that have multiple hydroxyl groups. Conversely, one can decrease the number of hydrogen bonding sites, or replace them with weaker hydrogen bonding atoms like nitrogen, to trap less. In contrast to the system studied here, one can design the head groups so they can donate hydrogen bonds, which can enhance entrapment of solutes like acetone that can only accept hydrogen bonds.

Finally, one can attempt to control the degree to which solutes coordinate with counterions. Increasing the valence of the counterions may cause them to bind more strongly to solutes which may be a useful way to trap carbonyl-containing solutes like urea for longer periods of time. Of course, an increased valence would require proportionately less total counter ions to balance the system charge which could result in the opposite effect. One could also design the head groups so that counterions are negatively charged which may eliminate their interaction with most solutes.

The findings here are likely too complex to point towards a clear design of an optimal LLC membrane for a particular separation. This work does demonstrate that there is a large range of solute-membrane interactions resulting from the chemically complex and inhomogeneous LLC membrane structure. The varying chemical functionality of the solutes themselves gives rise to an immense diversity of transport behavior. This behavior suggests that a large range of chemical selectivities may be possible in self-assembled nanoporous membranes. Atomistic modeling gives us the opportunity to observe these interactions at the molecular scale, at least approximately, so that we can think more critically about nanostructured membrane design.

## **Supporting Information**

Detailed explanations and expansions upon the results and procedures mentioned in the main text are described in the Supporting Information. This information is available free of charge via the Internet at <http://pubs.acs.org>.

## **Acknowledgments**

Molecular simulations were performed using the Extreme Science and Engineering Discovery Environment (XSEDE), which is supported by National Science Foundation (NSF) grant number ACI-1548562. Specifically, it used the Bridges system, which is supported by NSF award number ACI-1445606, at the Pittsburgh Supercomputing Center (PSC). This work also utilized the RMACC Summit supercomputer, which is supported by the NSF (awards ACI-1532235 and ACI-1532236), the University of Colorado Boulder, and Colorado State University. The Summit supercomputer is a joint effort of the University of Colorado Boulder and Colorado State University.

The authors thank Christopher Calderon and Gregory Morrin for helping kick start our studies of subdiffusive transport. Additionally, the authors thank Douglas Gin and Richard Noble for their guidance on past and present experimental research on LLC membranes and for reading over this manuscript before submission.

## References

- (1) Fritzmann, C.; Lwenberg, J.; Wintgens, T.; Melin, T. State-of-the-Art of Reverse Osmosis Desalination. *Desalination* **2007**, *216*, 1–76.
- (2) Schwarzenbach, R. P.; Escher, B. I.; Fenner, K.; Hofstetter, T. B.; Johnson, C. A.; Gunten, U. v.; Wehrli, B. The Challenge of Micropollutants in Aquatic Systems. *Science* **2006**, *313*, 1072–1077.
- (3) Dischinger, S. M.; Rosenblum, J.; Noble, R. D.; Gin, D. L.; Linden, K. G. Application of a Lyotropic Liquid Crystal Nanofiltration Membrane for Hydraulic Fracturing Flowback Water: Selectivity and Implications for Treatment. *J. Membr. Sci.* **2017**, *543*, 319–327.
- (4) Warsinger, D. M.; Chakraborty, S.; Tow, E. W.; Plumlee, M. H.; Bellona, C.; Lou-tatidou, S.; Karimi, L.; Mikelonis, A. M.; Achilli, A.; Ghassemi, A. et al. A Review of Polymeric Membranes and Processes for Potable Water Reuse. *Prog. Polym. Sci.* **2018**, *81*, 209–237.
- (5) Van Der Bruggen, B.; Vandecasteele, C.; Van Gestel, T.; Doyen, W.; Leysen, R. A Review of Pressure-Driven Membrane Processes in Wastewater Treatment and Drinking Water Production. *Environ. Prog.* **2003**, *22*, 46–56.
- (6) Hilal, N.; Al-Zoubi, H.; Darwish, N. A.; Mohamma, A. W.; Abu Arabi, M. A Comprehensive Review of Nanofiltration Membranes:treatment, Pretreatment, Modelling, and Atomic Force Microscopy. *Desalination* **2004**, *170*, 281–308.
- (7) Werber, J. R.; Osuji, C. O.; Elimelech, M. Materials for Next-Generation Desalination and Water Purification Membranes. *Nat. Rev. Mater.* **2016**, *1*, 16018.
- (8) Alexandridis, P.; Lindman, B. *Amphiphilic Block Copolymers: Self-Assembly and Applications*; Elsevier, 2000; Google-Books-ID: HsUuCbPeiUUC.

- (9) Zhou, M.; Kidd, T. J.; Noble, R. D.; Gin, D. L. Supported Lyotropic Liquid-Crystal Polymer Membranes: Promising Materials for Molecular-Size-Selective Aqueous Nanofiltration. *Adv. Mater.* **2005**, *17*, 1850–1853.
- (10) Dischinger, S. M.; McGrath, M. J.; Bourland, K. R.; Noble, R. D.; Gin, D. L. Effect of Post-Polymerization Anion-Exchange on the Rejection of Uncharged Aqueous Solutes in Nanoporous, Ionic, Lyotropic Liquid Crystal Polymer Membranes. *J. Membr. Sci.* **2017**, *529*, 72–79.
- (11) Smith, R. C.; Fischer, W. M.; Gin, D. L. Ordered Poly(p-phenylenevinylene) Matrix Nanocomposites via Lyotropic Liquid-Crystalline Monomers. *J. Am. Chem. Soc.* **1997**, *119*, 4092–4093.
- (12) Carter, B. M.; Wiesnauer, B. R.; Hatakeyama, E. S.; Barton, J. L.; Noble, R. D.; Gin, D. L. Glycerol-Based Bicontinuous Cubic Lyotropic Liquid Crystal Monomer System for the Fabrication of Thin-Film Membranes with Uniform Nanopores. *Chem. Mater.* **2012**, *24*, 4005–4007.
- (13) Hatakeyama, E. S.; Wiesnauer, B. R.; Gabriel, C. J.; Noble, R. D.; Gin, D. L. Nanoporous, Bicontinuous Cubic Lyotropic Liquid Crystal Networks via Polymerizable Gemini Ammonium Surfactants. *Chem. Mater.* **2010**, *22*, 4525–4527.
- (14) Chuysinuan, P.; Chimnoi, N.; Techasakul, S.; Supaphol, P. Gallic Acid-Loaded Electrospun Poly(L-Lactic Acid) Fiber Mats and their Release Characteristic. *Macromol. Chem. Phys.* **2009**, *210*, 814–822.
- (15) Perrin, D. D.; Dempsey, B.; Serjeant, E. P. *Pka Prediction for Organic Acids and Bases*; Chapman & Hall, 1981; OCLC: 876685660.
- (16) Bekker, H.; Berendsen, H. J. C.; Dijkstra, E. J.; Achterop, S.; van Drunen, R.; van der Spoel, D.; Sijbers, A.; Keegstra, H.; Reitsma, B.; Renardus, M. K. R. GROMACS:

A Parallel Computer for Molecular Dynamics Simulations. Physics Computing '92 ed. 1993.

- (17) Berendsen, H. J. C.; van der Spoel, D.; van Drunen, R. GROMACS: A Message-Passing Parallel Molecular Dynamics Implementation. *Comput. Phys. Commun.* **1995**, *91*, 43–56.
- (18) Van Der Spoel, D.; Lindahl, E.; Hess, B.; Groenhof, G.; Mark, A. E.; Berendsen, H. J. C. GROMACS: Fast, Flexible, and Free. *J. Comput. Chem.* **2005**, *26*, 1701–1718.
- (19) Hess, B.; Kutzner, C.; van der Spoel, D.; Lindahl, E. GROMACS 4: Algorithms for Highly Efficient, Load-Balanced, and Scalable Molecular Simulation. *J. Chem. Theory Comput.* **2008**, *4*, 435–447.
- (20) Wang, J.; Wolf, R. M.; Caldwell, J. W.; Kollman, P. A.; Case, D. A. Development and Testing of a General Amber Force Field. *J. Comput. Chem.* **2004**, *25*, 1157–1174.
- (21) Wang, J.; Wang, W.; Kollman, P. A.; Case, D. A. Automatic Atom Type and Bond Type Perception in Molecular Mechanical Calculations. *J. Mol. Graphics. Modell.* **2006**, *25*, 247–260.
- (22) Case, D.; Betz, R.; Botello-Smith, W.; Cerutti, D.; Cheatham, T., III; Darden, T.; Duke, R.; Giese, T.; Gohlke, H.; Goetz, A. et al. AmberTools16. 2016.
- (23) Zhou, M.; Nemade, P. R.; Lu, X.; Zeng, X.; Hatakeyama, E. S.; Noble, R. D.; Gin, D. L. New Type of Membrane Material for Water Desalination Based on a Cross-Linked Bicontinuous Cubic Lyotropic Liquid Crystal Assembly. *J. Am. Chem. Soc.* **2007**, *129*, 9574–9575.
- (24) Resel, R.; Theissl, U.; Gadermaier, C.; Zojer, E.; Kriechbaum, M.; Amenitsch, H.; Gin, D.; Smith, R.; Leising, G. The H2-Phase of the Lyotropic Liquid Crystal Sodium 3,4,5-Tris(omega-Acryloyloxyundecyloxy)benzoate. *Liq. Cryst.* **2000**, *27*, 407–411.

- (25) Coscia, B. J.; Yelk, J.; Glaser, M. A.; Gin, D. L.; Feng, X.; Shirts, M. R. Understanding the Nanoscale Structure of Inverted Hexagonal Phase Lyotropic Liquid Crystal Polymer Membranes. *J. Phys. Chem. B* **2019**, *123*, 289–309.
- (26) Meroz, Y.; Sokolov, I. M. A Toolbox for Determining Subdiffusive Mechanisms. *Phys. Rep.* **2015**, *573*, 1–29.
- (27) Metzler, R.; Jeon, J.-H.; Cherstvy, A. G.; Barkai, E. Anomalous Diffusion Models and Their Properties: Non-Stationarity, Non-Ergodicity, and Ageing at the Centenary of Single Particle Tracking. *Phys. Chem. Chem. Phys.* **2014**, *16*, 24128–24164.
- (28) Maginn, E. J.; Messerly, R. A.; Carlson, D. J.; Roe, D. R.; Elliott, J. R. Best Practices for Computing Transport Properties 1. Self-Diffusivity and Viscosity from Equilibrium Molecular Dynamics [Article v1.0]. *LiveCoMS* **2018**, *1*, 6324–.
- (29) Schultz, S. G.; Solomon, A. K. Determination of the Effective Hydrodynamic Radii of Small Molecules by Viscometry. *J. Gen. Physiol.* **1961**, *44*, 1189–1199.
- (30) Gierer, A.; Wirtz, K. Molekulare Theorie der Mikroreibung - Molecular Theory of Microfriction. *Z. Naturforsch* **1953**, *8*, 532–538.
- (31) Chen, H. C.; Chen, S. H. Diffusion of Crown Ethers in Alcohols. *J. Phys. Chem.* **1984**, *88*, 5118–5121.
- (32) Chan, T. C.; Li, H. T.; Li, K. Y. Effects of Shapes of Solute Molecules on Diffusion: A Study of Dependences on Solute Size, Solvent, and Temperature. *J. Phys. Chem. B* **2015**, *119*, 15718–15728.
- (33) Lee, H.; Venable, R. M.; MacKerell, A. D.; Pastor, R. W. Molecular Dynamics Studies of Polyethylene Oxide and Polyethylene Glycol: Hydrodynamic Radius and Shape Anisotropy. *Biophys. J.* **2008**, *95*, 1590–1599.

- (34) He, L.; Niemeyer, B. A Novel Correlation for Protein Diffusion Coefficients Based on Molecular Weight and Radius of Gyration. *Biotechnol. Progr.* **2003**, *19*, 544–548.
- (35) Li, Z. Critical Particle Size Where the Stokes-Einstein Relation Breaks Down. *Phys. Rev. E* **2009**, *80*, 061204.
- (36) Truong, C.; Oudre, L.; Vayatis, N. Ruptures: Change Point Detection in Python. *arXiv* **2018**, *arXiv:1801.00826*.
- (37) Efron, B.; Tibshirani, R. J. *An Introduction to the Bootstrap*; CRC Press, 1994; Google-Books-ID: gLlpIUxRntoC.
- (38) Luzar, A.; Chandler, D. Effect of Environment on Hydrogen Bond Dynamics in Liquid Water. *Phys. Rev. Lett.* **1996**, *76*, 928–931.
- (39) Prada-Gracia, D.; Shevchuk, R.; Rao, F. The Quest for Self-Consistency in Hydrogen Bond Definitions. *J. Chem. Phys.* **2013**, *139*, 084501.
- (40) Rowley, C. N.; Roux, B. The Solvation Structure of Na<sup>+</sup> and K<sup>+</sup> in Liquid Water Determined from High Level ab Initio Molecular Dynamics Simulations. *J. Chem. Theory Comput.* **2012**, *8*, 3526–3535.
- (41) Starr, F. W.; Nielsen, J. K.; Stanley, H. E. Fast and Slow Dynamics of Hydrogen Bonds in Liquid Water. *Phys. Rev. Lett.* **1999**, *82*, 2294–2297.
- (42) Martiniano, H. F. M. C.; Galamba, N. Insights on Hydrogen-Bond Lifetimes in Liquid and Supercooled Water. *J. Phys. Chem. B* **2013**, *117*, 16188–16195.
- (43) Voloshin, V. P.; Naberukhin, Y. I. Hydrogen Bond Lifetime Distributions in Computer-Simulated Water. *J. Struct. Chem.* **2009**, *50*, 78–89.
- (44) Mahoney, M. W.; Jorgensen, W. L. Diffusion Constant of the Tip5p Model of Liquid Water. *J. Chem. Phys.* **2000**, *114*, 363–366.

- (45) Carvajal, C.; Tlle, K. J.; Smid, J.; Szwarc, M. Studies of Solvation Phenomena of Ions and Ion Pairs in Dimethoxyethane and Tetrahydrofuran. *J. Am. Chem. Soc.* **1965**, *87*, 5548–5553.
- (46) Wu, X.; Jin, S.; Zhang, Z.; Jiang, L.; Mu, L.; Hu, Y.-S.; Li, H.; Chen, X.; Armand, M.; Chen, L. et al. Unraveling the Storage Mechanism in Organic Carbonyl Electrodes for Sodium-Ion Batteries. *Sci. Adv.* **2015**, *1*, e1500330.
- (47) Shinoda, T.; Ogawa, H.; Cornelius, F.; Toyoshima, C. Crystal Structure of the SodiumPotassium Pump at 2.4 Resolution. *Nature* **2009**, *459*, 446–450.
- (48) Srinivas, G.; Bhattacharyya, S.; Bagchi, B. Computer Simulation and Mode Coupling Theory Study of the Effects of Specific SoluteSolvent Interactions on Diffusion: Crossover from a Sub-Slip to a Super-Stick Limit of Diffusion. *J. Chem. Phys.* **1999**, *110*, 4477–4482.
- (49) Biswal, H. S. In *Noncovalent Forces*; Scheiner, S., Ed.; Challenges and Advances in Computational Chemistry and Physics; Springer International Publishing: Cham, 2015; pp 15–45.

# TOC Graphic

